9th International Conference on Numerical Ship Hydrodynamics
Ann Arbor, Michigan, August 5-8, 2007

Evaluation of an URANS-LES Hybrid Approach for Turbulent Free Surface Flows around Surface-Piercing Bodies

Sung-Eun Kim[1] and Davor Cokljat[2]
([1]Naval Surface Warfare Center, Carderock Division, U.S.A.)
([2]ANSYS Incorporated, Sheffields, U.K.)

ABSTRACT

A hybrid turbulence modeling approach combining unsteady Reynolds-averaged Navier-Stokes (URANS) equation-based modeling and large eddy simulation (LES) is applied to turbulent free-surface flows around surface-piercing bodies involving wave-breaking and bubble formation. Based on a two-equation k-ε turbulence model, the hybrid model reduces to a RANS turbulence model or a subgrid-scale turbulence model depending on the local mesh resolution (filter size) and the local integral turbulence length-scale. The computations were carried out using a second-order-accurate finite-volume Navier-Stokes solver that permits use of arbitrary unstructured meshes and local mesh refinement. Volume-of-fluid (VOF) method was employed to capture the free-surface. The URANS-LES hybrid approach is shown to reproduce the salient features of the turbulent free-surface flows around the surface-piercing bodies with reasonable accuracy on relatively coarse meshes on which the fidelity of LES degrades.

INTRODUCTION

One of the difficulties encountered in numerically predicting turbulent free-surface flows comes from turbulence modeling. Turbulent structure near free-surface is markedly different from those in regions away from free-surface. Anisotropy of turbulence and energy backscatter are among much discussed features of free-surface turbulence (e.g., Shen and Yue, 2001). In this respect, free-surface turbulence shares its characteristics with near-wall turbulence. And yet, the physics of free-surface turbulence widely varies depending on Froude number and Weber number (see Brocchini and Peregrine, 2001). For violent free-surface flows around surface-piercing bodies involving wave-induced flow separation, wave-breaking, and bubble formation, it is a formidable task to gain even a qualitative understanding of interactions among surface waves, boundary layer, wake, and their effects on free-surface turbulence, let alone to find any models reflecting those effects. Adds to all this the difficulty of modeling the physics of turbulence associated with interfacial transfer of mass, momentum, and kinetic energy occurring in two-phase flows. Given the challenges, it is not difficult to see why Reynolds-averaged Navier-Stokes (RANS) equations-based turbulence modeling is considered less than adequate for this class of free-surface flows.

Large eddy simulation (LES) has been considered to be fundamentally more suitable for the subject flow, in view of the dominant role played by large-scale turbulent structures. Dommermuth and Novikov (1993), Shen and Yue (2001), Kawamura *et a*l. (2002), Yue *et al.* (2005), and most recently Kim and Rhee (2006) are among those who attempted LES for simulation of turbulent free-surface flows. For all the merits of LES for flows, LES is computationally intensive, often prohibitively. Despite the remarkable increase in computational power in terms of hardware and software. Alleviating the cost of LES is an area of active research these days. The first fruit of such efforts came in the so-called Detached Eddy Simulation (DES) approach proposed by Spalart *et al.* (1997). In broad terms, DES sets out to selectively use either RANS or subgrid-scale (SGS) turbulence modeling in the flow domain in question based on certain criterion. The turbulence model adopted in Spalart's DES approach reduces to the Spalart and Allmaras' eddy-viscosity transport (RANS) model in near-wall region, whereas it reduces to a subgrid-scale (SGS) turbulence model away from wall. This earliest version of DES approaches allows one to use highly stretched meshes in attached boundary for use with the RANS modeling, which significantly saves cell counts and, as a consequence, reduce the computational cost

The present study is a sequel to the earlier LES study by the authors (Kim and Rhee, 2006). What we tried to do here in this study is to critically

evaluate a URANS/LES hybrid turbulence modeling approach for turbulent free-surface flows around surface-piercing bodies. The hybrid model is based on two-equation k-ε turbulence model. The same numerical methods and algorithms were used as in the previous study. Free-surface is resolved with volume-of-fluid (VOF) method. The same surface-piercing hydrofoil is considered with a rectangular plan-form and NACA-0024 cross-section experimentally studied in the towing tank at the University of Iowa (Zhang and Stern, 1996; Metcalf *et al.*, 2006). We considered the case of $Fr = 0.37$ in this study. The corresponding Reynolds numbers ($\mathrm{Re} = U_0 c/\nu$) are 1.52×10^6. In addition, the flow around a surface-piercing circular cylinder was newly considered in this study, which was experimentally studied by Inoue *et al.* (1993). LES as well as DES computations have been carried out for the circular cylinder case at the Froude number (Fr) of 0.8, with the corresponding Reynolds number of $Re = 2.7 \times 10^4$.

The computations have been carried out using a parallelized, finite-volume Navier-Stokes solver that is second-order accurate in time and space.

GOVERNING EQUATIONS\

The governing equations solved in DES are a single set of the filtered (averaged) Navier-Stokes equations that are shared by gas (air) and liquid (water) phases or their mixture.

The filtered Navier-Stokes equations can be written as

$$\frac{\partial \overline{\rho}}{\partial t} + \frac{\partial}{\partial x_j}\left(\overline{\rho}\overline{u}_j\right) = 0 \tag{1}$$

and

$$\frac{\partial}{\partial t}\left(\overline{\rho}\overline{u}_i\right) + \frac{\partial}{\partial x_j}\left(\overline{\rho}\overline{u}_i\overline{u}_j\right) = -\frac{\partial \overline{p}}{\partial x_i} + \frac{\partial}{\partial x_j}\left\{\left(\mu + \mu_t\right)\left(\frac{\partial \overline{u}_i}{\partial x_j} + \frac{\partial \overline{u}_j}{\partial x_i}\right)\right\} \tag{2}$$

where the overbar denotes the filtering operation, p the piezometric pressure ($p = p_s + \rho g z$).

The presence of two phases (air and water) in the computational domain is represented by volume fraction, $\gamma(\mathbf{x},t)$ (Harlow and Welch, 1965). Volume-fraction in intermittent two-phase flows can be interpreted as a volume-averaged intermittency function, $I(\mathbf{x},t)$ whose value takes either 0 or 1 depending on whether the point ($\mathbf{x}$) in question is in water or air. Thus,

$$\gamma(\mathbf{x},t) \equiv \overline{I(\mathbf{x},t)} \equiv \frac{1}{V_c}\iiint_{V_c} I(\mathbf{x},t)\,dV \tag{3}$$

Note that the volume-fraction changes in both space and time, whose value ranges between 0 and 1. Volume-fraction is obtained from its transport equation

$$\frac{\partial \gamma}{\partial t} + \frac{\partial}{\partial x_j}\left(\gamma \overline{u}_j\right) = 0 \tag{4}$$

The physical properties such as density and dynamic viscosity are computed as functions of γ from

$$\begin{aligned} \rho &= (1-\gamma)\rho_w + \gamma\rho_a \\ \mu &= (1-\gamma)\mu_w + \gamma\mu_a \end{aligned} \tag{5}$$

where the subscripts "a" and "w" denote air and water, respectively.

Insofar as the fluid density fluctuates in the vicinity of free-surface with the volume-fraction, the filtered variables in Equation (1) and Equation (2), except the density, can be interpreted as density-weighted (Favre-averaged) variables as employed for compressible flows.

NUMERICAL METHOD

The computations were carried out using a development version of FLUENT V6.3. FLUENT employs a cell-centered finite-volume method based on a multi-dimensional linear reconstruction scheme that permits use of computational elements (cells) with arbitrary polyhedral cell topology including quadrilateral, hexahedral, triangular, tetrahedral, pyramidal, prismatic, and hybrid meshes. The solution gradients at cell centers are obtained by applying Green-Gauss theorem based on a node-based quadrature (Kim *et al.*, 2003). In the present study, the discretization schemes and the solution algorithms were judiciously chosen to ensure accuracy, efficiency and stability of the numerical solutions, all of which are essential for successful LES. For discretization of convection terms in the filtered momentum equations, we adopted a *bounded* central-differencing (BCD) scheme that is essentially non-dissipative, second-order-accurate central-differencing scheme combined with a nonlinear flux-limiter activated only when and where needed to suppress numerical oscillations. For discretization of advection term in the VOF equation, we employed a modified high resolution interface-capturing (HRIC) scheme that is compressive and therefore ideally suited for resolving sharp interface. Surface tension effect is included using the continuum

surface force (CSF) model that effectively represents surface tension as a volumetric source (forcing) term in the momentum equations.

The system of discretized governing equations is solved using point-implicit Gauss-Seidel relaxation along with algebraic multi-grid (AMG) method to accelerate solution convergence. The N-S solver and the SGS turbulence model are fully parallelized using MPI.

An implicit fractional-step method (Kim and Makarov, 2005) in combination with a second-order accurate, three-level backward-differencing scheme for time-discretization was employed to advance the solution in time. Unlike explicit schemes, implicit time-advancement scheme allows one to take as large a time-step size as needed to guarantee a desired temporal resolution, bringing a considerable speed-up in simulations of transient flows. In this algorithm, the momentum equations are decoupled from the continuity equation using an approximate factorization of the coupled Navier-Stokes equations.

In the present computations, the volume-fraction equation was solved first in the beginning of each time-step, which is followed by the remaining steps with the newly updated physical properties of the mixture.

TURBULENCE MODELING

The DES method originally proposed by Spalart *et al.* (1997) has been widely used for aerodynamics applications (Nikitin *et al.*, 2000; Travin *et al.*, 2000; Cokljat and Liu, 2002; Spalart *et al.*, 2003). An interesting study had been conducted for an A-airfoil for the LESFOIL European project. The DES study of Cokljat and Liu (2002) showed an excellent agreement despite the relatively coarse mesh used for the DES computation. To obtain a similar accuracy on the same flow using LES, a substantially larger mesh had to be used (Mary and Sagaut, 2002).

In spite of its encouraging performance for massively separated flows, DES for attached flows, e.g. channel flows (e.g. Nikitin *et al.*, 2000), showed a fairly strong dependency on grid resolution. In that work, the skin-friction coefficient was underpredicted by about 15 %. Furthermore, DES simulations on separated flows as studied by Travin *et al.* (2000) also revealed various short comings. One of the main drawbacks of DES approaches in general lies with the interface region between RANS zone and LES zone where two completely different turbulence models are to be matched.

Strelets (2000) performed DES computations of several massively separated flows using a new hybrid model based on the k-ω SST model. This two-equation-based hybrid model offers two potential advantages compared to the original DES approach of Spalart *et al.* (1997). Firstly, modern two-equation-based RANS models provide better accuracy than the one-equation model – or lower-order turbulence models - for a wide range of flows including boundary layers, wakes, and other free shear flows. Thus, the DES approach based on advanced two-equation turbulence models would benefit from the superior performance of the advanced RANS models. Secondly, unlike the one-equation based DES model, the demarcation of RANS and LES regions in the two-equation-based DES approach is not any more based on the proximity to wall (wall distance) only. Two-equation RANS turbulence models such as k-ε or k-ω models give an estimate of integral length-scale of turbulence that can be used to determine whether to invoke subgrid-scale turbulence model or RANS turbulence model. The decision is based on upon the integral length-scale and the grid-filter size.

Among many hybrid RANS/LES models available, we picked the DES approach based on realizable k-ε turbulence model Shih et al. (1995). The modeled transport equation for k in this model is given by:

$$\frac{\partial}{\partial t}(\overline{\rho}k)+\frac{\partial}{\partial x_j}(\overline{\rho}k\overline{u}_j)=\frac{\partial}{\partial x_j}\left[\left(\mu+\frac{\mu_t}{\sigma_k}\right)\frac{\partial k}{\partial x_j}\right] + P_k-\frac{\rho k^{3/2}}{l_{DES}} \qquad (6)$$

where P_k is the production of turbulent kinetic energy, and the last term on r.h.s. of the above equation is modified dissipation rate formulation used in conjunction with the present DES approach. The turbulent length scale is defined as:

$$l_{DES} = MIN\,(k^{3/2}/\varepsilon, C_{DES}\Delta) \qquad (7)$$

where Δ is the grid length-scale. C_{DES} is calibration constant and the value of 0.61 is adopted in the present study and Δ is the grid length scale computed from $\Delta = \sqrt[3]{V}$ where V is the volume of the cell. The transport equation for ε was taken from the realizable k-ε equation of Shih *et al.* (1995).

For the LES computations for the circular cylinder case, the same dynamic Smagorinsky model was used as the one employed in the earlier study of the authors (Kim and Rhee, 2006).

COMPUTATIONAL DOMAIN AND MESH

Circular cylinder

The upstream inlet boundary and the downstream exit boundary were placed at 8.5D and 20.5D forward and aft from the cylinder center, respectively. The lateral boundary is 5.0D away from the cylinder axis. The top and the bottom boundaries of the domain were placed at 2.0D and *5.0D* above and below the undisturbed free-surface, respectively. The blockage ratio of the cylinder (H/D, where H is the height of the domain) is approximately 4.8 %.

In order to quantify the mesh-dependency, the computations were made with two meshes with 1.5 million and 2.7 million elements.

Hydrofoil

The computational domain is bounded by an upstream inlet, a downstream exit, top and bottom planes, and a pair of far-field boundaries in the lateral direction. The upstream inlet boundary and the downstream exit boundary were placed at 3.0 chord-lengths (c) and 8.54 chord-lengths forward and aft from the leading-edge of the hydrofoil, respectively. The top and the bottom boundaries of the domain were placed at 0.21 c and *2.5 c* above and below the undisturbed free-surface, respectively. The lateral boundaries are at 5.0 c from the foil center-plane.

In view of the relatively simple geometry, block-structured hexahedral meshes with a C-H topology were used in this study. Two meshes were used in this study. The coarse mesh has 1.8 million elements, and the fine mesh has 4.7 million cells. The fine mesh was generated by locally refining all the cells in the coarse mesh in the strip between z = -0.15c and z = 0.1c. The near-wall mesh resolution for the 4.7 million cell mesh is such that the distance from the cylinder surface at the wall-adjacent cells is in the neighborhood of 3×10^{-4} chord-length, which translates to y^+ in the range of 3 ~ 35, yet staying close to y^+ = 10 on most of the foil surface. The fine mesh has twice finer than the coarser mesh in the near-wall region.

BOUNDARY CONDITIONS AND OTHER COMPUTATIONAL DETAILS

For both the circular cylinder and the hydrofoil case, on the upstream and lateral inlet boundaries, total pressure is specified. On these "pressure-inlet" boundaries supported in FLUENT, velocity is determined from the specified total pressure using the dynamic pressure and the hydrostatic pressure at given vertical location, and volume fraction values are simply extrapolated. At the downstream exit boundary, the hydrostatic pressure is determined from the depth below the free-surface, while other variables including volume-fraction are extrapolated. On the top and bottom boundaries, symmetry condition is imposed. On the foil surface, we employed a generalized wall-function approach that invokes proper wall-laws depending on the y^+ value at wall-adjacent cells. Thus, the wall model is applicable to the entire inner layer including the viscous sub-layer, buffer zone, and logarithmic layer.

The non-dimensional time-step size (Δt) used for the computations is 0.0002 sec. The time-step size was determined based on the estimates of the characteristic length and time scales of the eddy size to be resolved. The smallest time-scale to be resolved was computed from $\tau = \ell / u'$, where ℓ was taken as 0.02 c, and u' as $0.5U_0$. From these rough estimates, one turnover of the smallest resolved eddies will be resolved with roughly 200 time steps.

To shorten the initial transient period of the solution and to quickly attain statistically stationary state, we took steady RANS solution as the initial condition.

RESULTS

Circular cylinder

The results for the circular cylinder case obtained with the fine mesh (2.7M cell) mesh for Re = 2.8 x 10^4, and Fr = 0.8 are discussed here. An overall impression of the free-surface around the circular cylinder predicted by the DES is shown in Figure 1, along with that obtained using LES reported earlier (Kim and Rhee, 2006). The bow wave and the downstream wave pattern arising from the interaction between the turbulent wake and the free-surface are well captured by the DES. As evident in the figures, a vigorous aeration (ventilation) takes place in the near-wake. As observed in the LES, large air bubbles were seen to be entrained down to nearly 0.7D below the undisturbed free-surface in the DES results. Some of the vertically oriented vortices leave whirls on the free-surface with conspicuous depression around their cores. Overall, the DES results closely resemble the LES results. However, the flow structures predicted by DES appear to be slightly more coarse-grained than what the LES yields. In addition, the depression of the free-surface predicted by the DES seems smaller than the LES prediction.

Figure 2 shows the contours of time-averaged elevation of the free-surface (γ = 0.5) computed from the experiment (Inoue *et al.*, 1993). In Figure 3 are depicted the time-averaged free-surface elevations predicted by the DES and the LES. It is seen that the

main features of the free-surface elevation are well captured by the DES computation such as the wave pattern and height in front of the cylinder and in the wake. However, the contours clearly show that the depression of the free-surface predicted by DES is appreciably smaller than the LES prediction, especially in the near-wake region and in the shoulder wave region.

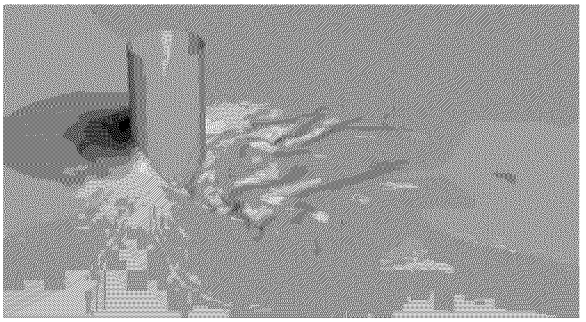

(a) DES

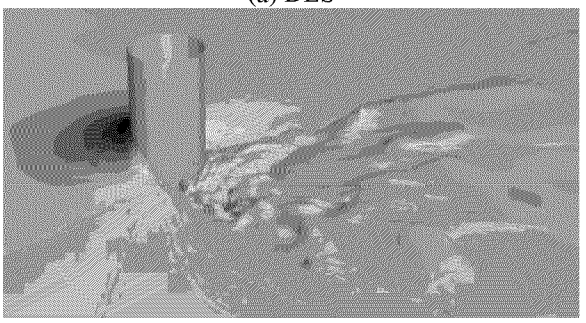

(b) LES

Figure 1. Instantaneous free-surface generated by the flow around a surface-piercing circular cylinder, colored by the surface elevation (Re = 2.8 x 10^4, Fr = 0.8)

Figure 4 are shows the time-averaged wave profiles in the spanwise (y) direction at two axial locations (x/D = 0.9, 2.0), predicted by the DES and the LES. Considering that the free-surface violently fluctuate, and as a result, the width of the surface-layer becomes large, the predicted profiles are plotted for the volume-fraction values of $\bar{\gamma}$ = 0.3, 0.4, 0.5. The large band-width of the time-averaged surface elevation for the range of volume-fraction, especially in the near-wake of the cylinder (x/D < 1.0), is an indication of large fluctuation of the free-surface and vigorous ventilation occurring near the free-surface.

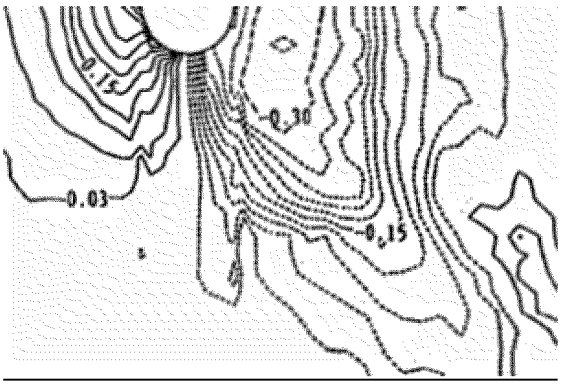

Figure 2. Contours of the time-averaged free-surface elevation (Re = 2.8 x 10^4, Fr = 0.8) measured by Inoue *et al.* (1993)

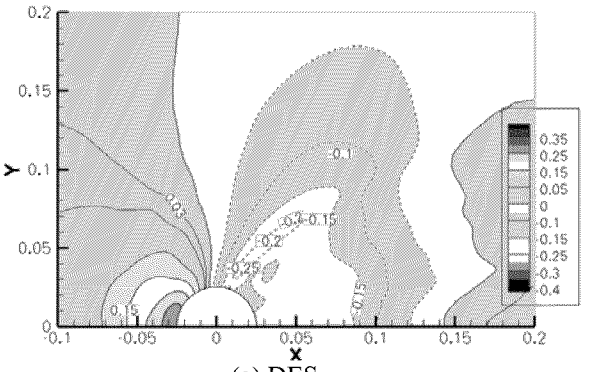

(a) DES

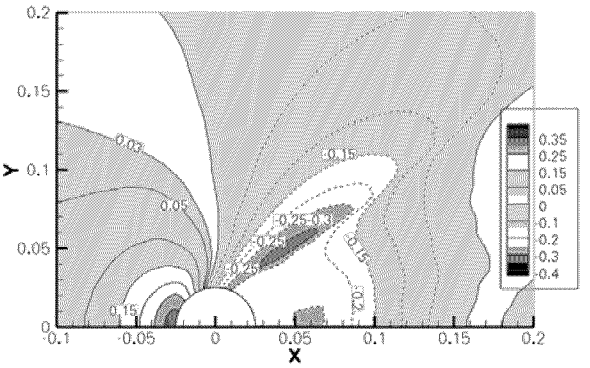

(b) LES

Figure 3. Contours of the time-averaged free-surface elevation (Re = 2.8 x 10^4, Fr = 0.8): (a) DES prediction; (b) LES prediction

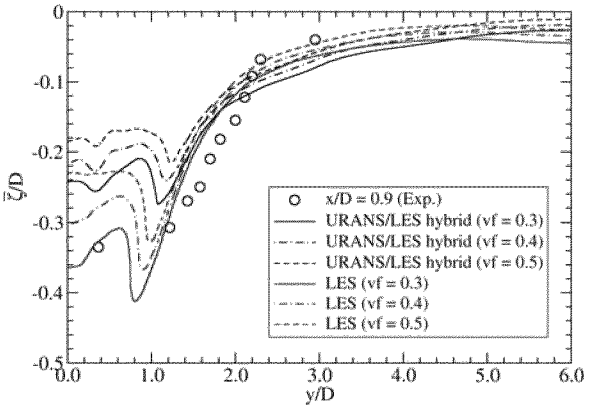

(a) x/D = 0.9

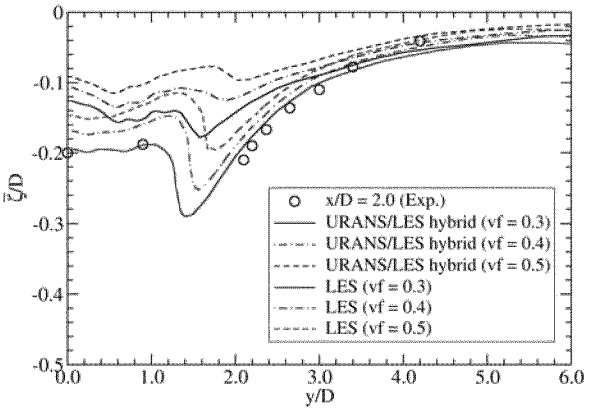

(b) x/D = 2.0

Figure 4. Time-averaged free-surface elevation (Re = 2.8 x 10^4, Fr = 0.8) at two axial locations (x/D = 0.9, 2.0). Note that the predictions for three different values of volume–fraction are shown.

Figure 4 show that the DES yields substantially smaller depression of the free-surface in the wake region than the LES prediction. One observation worthy of mentioning here with regard to the smaller depression of the free-surface in the near-wake predicted by the DES is that the DES prediction also gave a depth-averaged drag coefficient of around 0.5, a much smaller value than the LES prediction (C_D = 0.95) and the experimental correlation (C_D = 1.0). Although not shown here, the DES prediction yielded a substantially narrower wake than the LES prediction. In view of the fact that DES model reduces to RANS turbulence model in the near-wall region, the RANS turbulence model (realizable k-ε) used in this particular DES approach is most likely to blame for the discrepancy observed. Indeed, efficacy of DES – URAS/LES hybrid approaches - would surely hinge upon the performance of RANS turbulence models they adopt.

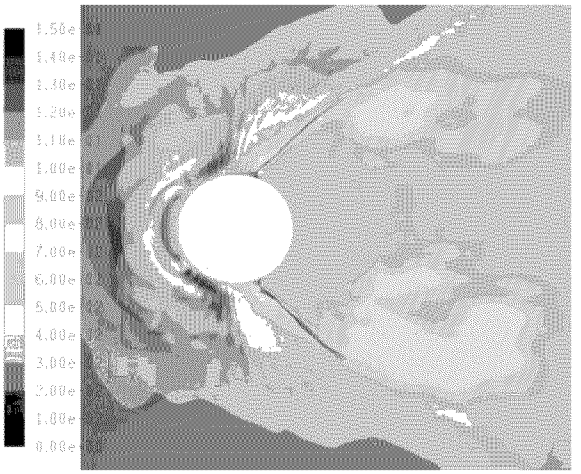

(a)DES

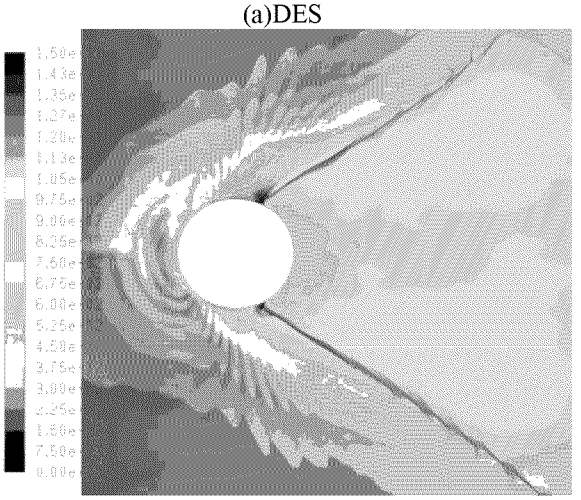

(b) LES

Figure 5. Contours of the r.m.s. vertical velocity fluctuation on the free surface (Re = 2.8 x 10^4, Fr = 0.8): top – predicted by the present DES and LES

Figure 5 depicts the contours of the r.m.s. vertical (z-) velocity fluctuation plotted on the mean free-surface predicted by the DES and the LES computations, which give an useful information on the r.m.s. free-surface elevation fluctuation. What these contour plots indicate is that the DES considerably dampens the normal velocity fluctuation in the wake in comparison to the LES prediction. As we will see later, this is also the case with the hydrofoil case.

In summary, the DES appears to predict the gross features of the turbulent free-surface flow around a surface-piercing circular cylinder with a reasonable accuracy. However, it tends to under-predict the depression of the free-surface in the wake and the level of the fluctuation of the free-surface.

Hydrofoil

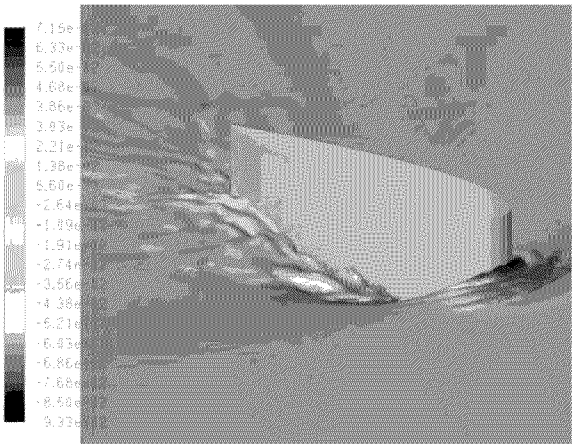

(a) DES

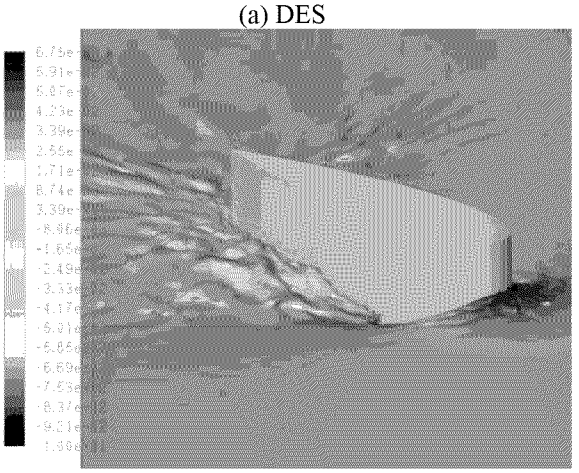

(b) LES

Figure 6. Instantaneous surface elevation around the surface-piercing hydrofoil predicted by the RANS/LES hybrid model and LES at $Fr = 0.37$

An overall impression of the free-surface around the surface-piercing hydrofoil predicted using the present DES approach is shown in Figure 6 along with the LES prediction for comparison. The instantaneous surface elevations were visualized using iso-surface of volume-fraction for $\gamma = 0.5$. The main characteristics of the free-surface portrayed in these figures closely resemble what is shown in the photographs taken in the experiment (Figure 6 in Metcalf *et al.*, 2006). They are also qualitatively similar to those observed by Pogozelski and Katz (1997) with the free-surface around a surface-piercing strut. The main difference between the DES and the LES predictions is the degree of details of the flow resolved by the predictions. The LES prediction appears to capture finer scales of motion compared to the DES result, most likely because the DES model reduces to a RANS turbulence model in some regions.

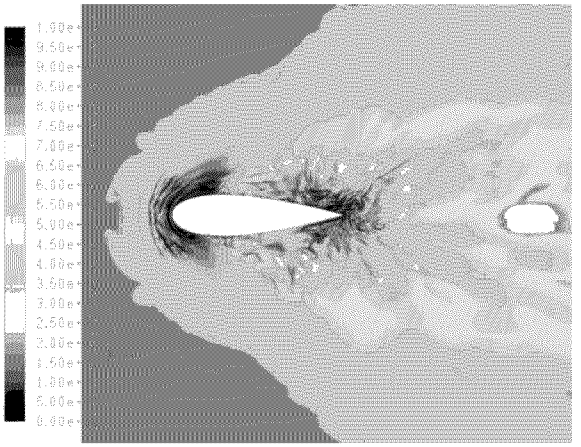

(a) DES

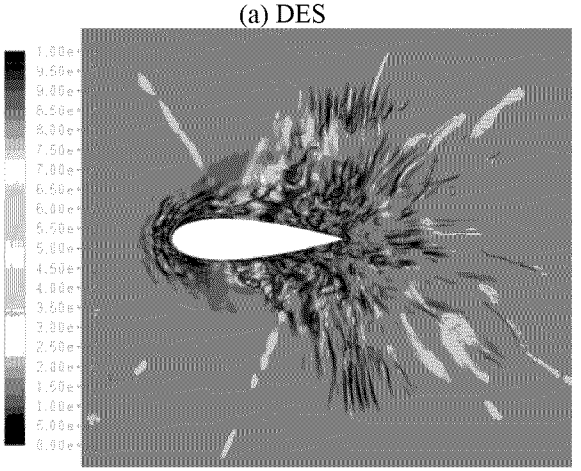

(b) LES

Figure 7. Ratio of turbulent iscosity to molecular viscosity (ν_t/ν) – plotted in the range of $0 < \nu_t/\nu < 1000$

In Figure 7 is shown the comparison of the ratio of turbulent viscosity to molecular viscosity at an instance of time. Not surprisingly, the DES approach yields much higher – by up to roughly two orders of magnitude - turbulent viscosity in regions away from the hydrofoil. This is an indication that the DES effectively reverts back to RANS turbulence model (realizable k-ε model in this study) in some parts of the flow domain.

How the solution domain, at an instance of time, is demarcated into RANS and LES regions is visualized in Figure 8 using a color map constructed using the size of the integral length scale of turbulence relative to the length-scale of the grid. In the figure, the RANS region is shown in blue,

whereas the LES region is depicted in red. With a caveat in mind that the demarcation is shown near the free-surface, the color map indicates that the RANS region resides in the thin boundary layer region near the hydrofoil and in the region far way from the hydrofoil. The LES region is between the two regions. One important point to stress here is that the RANS region in the far field could have not been recovered by the original DES of Spalart *et al.* (1997) which is based on the relative size of wall distance to grid spacing as the only demarcation criterion.

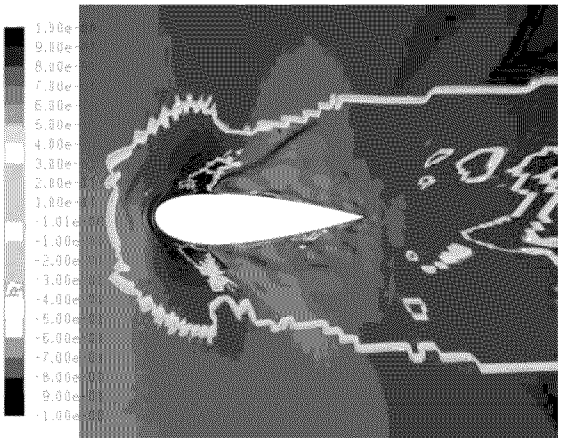

Figure 8. Color map showing demarcation of RANS and LES region – The RANS region is shown in blue, and the LES region in red.

Figure 9 shows the contours of instantaneous longitudinal vorticity component at a cross-flow plane ($x/c = 0.7$) predicted by the DES and the LES. The free-surface is also shown in these figures in solid lines near the top of each figiure. These contour plots shed light on the strength and the length scale of the subsurface vortical structure. The LES (Kim and Rhee, 2006), shown in Figure 9(b) reproduce the characteristic features of the subsurface vortical structures such as the extent and the length-scales of the vortices and the occurrence of pairs of counter-rotating vortices observed by Pogozelski and Katz (1997). The DES prediction appears to be qualitatively similar to the vortical structures pictured by the LES. However, the LES prediction exhibits a far richer feature than the DES result. In addition, the vorticity predicted by the DES is much weaker than the LES prediction.

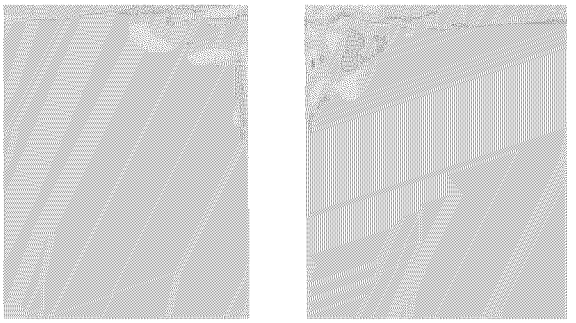

(a) DES

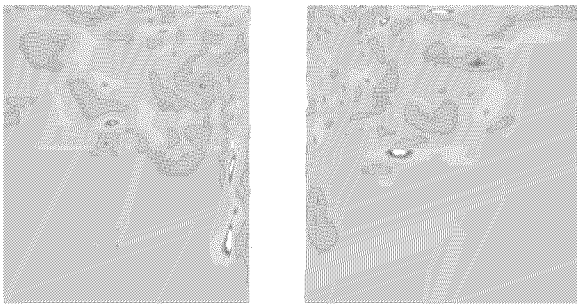

(b) LES (Kim and Rhee, 2006)

Figure 9. Contour of instantaneous axial vorticity component (ω_x) between $-100 < \omega_x < 100$ viewed from upstream

Figures 10 show the contours of the x-component of the time-averaged wall-shear stress on the hydrofoil surface predicted by the DES, which clearly indicates that there is a pocket of flow reversal (under the mean free-surface - a wedge-shaped region below the mean free-surface, colored in blue in the figure. The LES reported earlier also captured the wedge-shaped region of flow reversal. The contour of the wall-shear indicates that the flow underneath the pocket of separation, being accelerated past the bow and the shoulder driven by strong favorable pressure gradient, penetrates deeply under the free-surface and remains attached nearly to the trailing-edge. The extent and the topological structure of the flow separation are largely consistent with those described by Zhang and Stern (1996) and Pogozelski and Katz (1997).

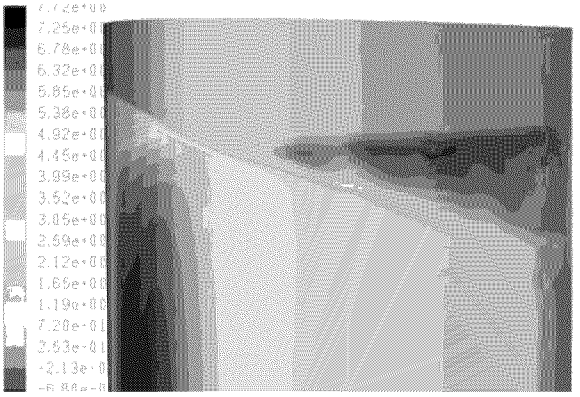

Figure 10. Contour of the time-averaged x-component of the wall-shear stress on the hydrofoil surface predicted by the present DES

Figure 11 shows the contour of the time-averaged free-surface elevation predicted by the DES on the fine mesh (4.7 million cell), along with the measurement (Metcalf *et al.* 2006). The DES prediction closely matches the measured elevation. The Kelvin waves away from the hydrofoil are closely reproduced by the DES prediction, in terms of the height and the position of the wave crests and troughs and the divergence angle of the waves. The DES apparently overpredicts the surface elevation in the central portion of the near-wake, as compared to the measurement. Nonetheless, the present DES result is quite promising.

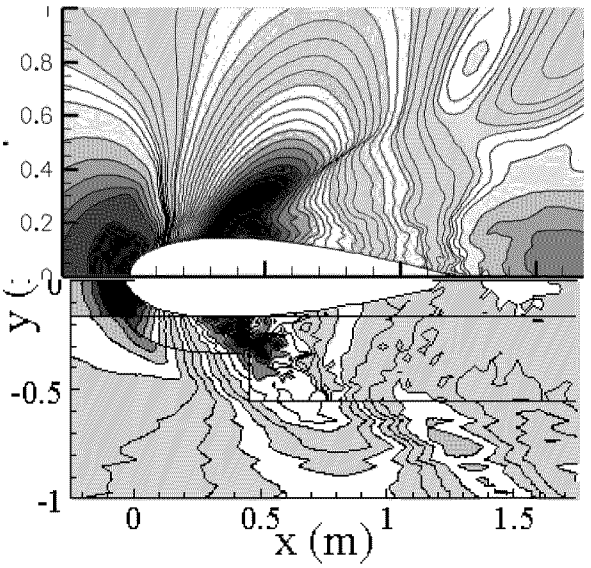

Figure 11. Time-averaged free-surface wave elevation predicted by the present DES at Fr = 0.37 Top – prediction (fine mesh); Bottom – measured.

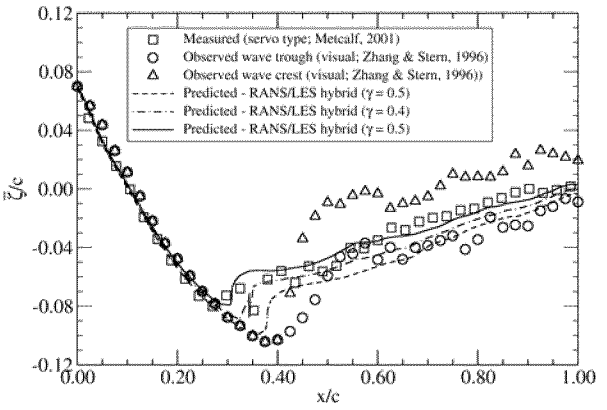

(a) DES

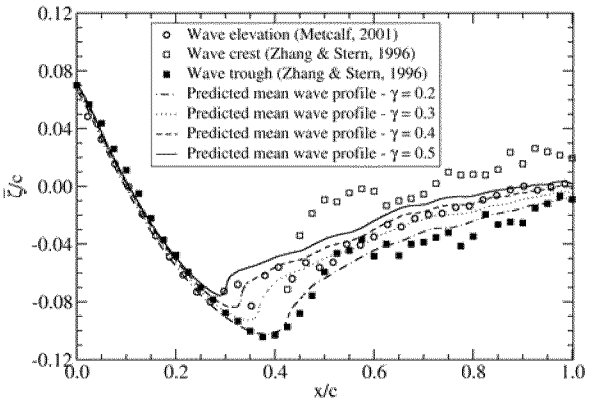

(b) LES (Kim and Rhee, 2006)

Figure 12. Time-averaged wave profiles along the hydrofoil foil surface predicted by (a) DES; (b) LES

Figures 12(a) and 12(b) depict the wave profiles along the hydrofoil surface predicted by the DES and the LES, respectively, along with the ones determined experimentally (Zhang and Stern, 1996; Metcalf *et al.*, 2006). The time-averaged wave profiles are shown in Figures for a few different values of volume-fraction; γ = 0.2, 0.3, 0.4, and 0.5. It should be stressed that the large band-width of the wave elevations for the mean volume-fraction ranging from γ = 0.2 to γ = 0.5 is an evidence of the large fluctuation of wave elevation and the occurrence of intermittent two-phase flow in the separated region and in the near-wake. It is seen that, in terms of the time-averaged wave profiles along the body surface (near-field), the DES results closely match the LES predictions. The mean wave profile measured by the servo-driven wave gage differs significantly from those determined by the visual observations. The DES and the LES predictions for γ = 0.5 agree well with the time-averaged wave gage data. And, the mean wave profiles for γ = 0.2 predicted by both the DES and the LES are seen to be close to the wave trough visually determined using markers and video.

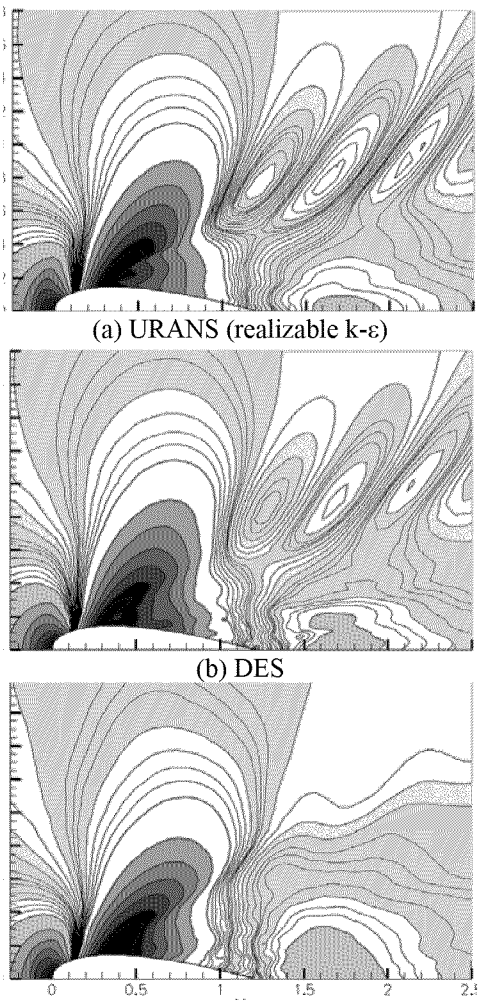

(a) URANS (realizable k-ε)

(b) DES

(c) LES

Figure 13. Comparison of the time-averaged free-surface elevation predictions by URANS, DES, and LES at Fr = 0.37 on the coarse mesh (1.8 million cells)

Thus far, we have shown and discussed the DES predictions, making comparisons with the earlier LES predictions whenever possible. Looking at both the DES and the LES predictions, side by side, on the same fine mesh (4.8 million cells) help us to delineate what DES vis-à-vis LES can offer for the subject flow. To further investigate how URANS, DES, and LES would fare with one another, we conducted URANS, DES, and LES computations, on the coarser mesh with 1.8 million cells. The resolution of the coarse mesh is roughly is half the resolution of the fine mesh used for the DES computations presented so far. The mean free-surface elevations predicted using the three different approaches are shown in Figure 13. Interestingly enough, yet not surprisingly, the URANS result obtained with the realizable k-ε model yields the most pronounced Kelvin wave system. The DES captures the Kelvin waves, although the wave crests and troughs are slightly less pronounced than the RANS prediction. The most remarkable observation is that LES on this coarse mesh fail to resolve the Kelvin waves.

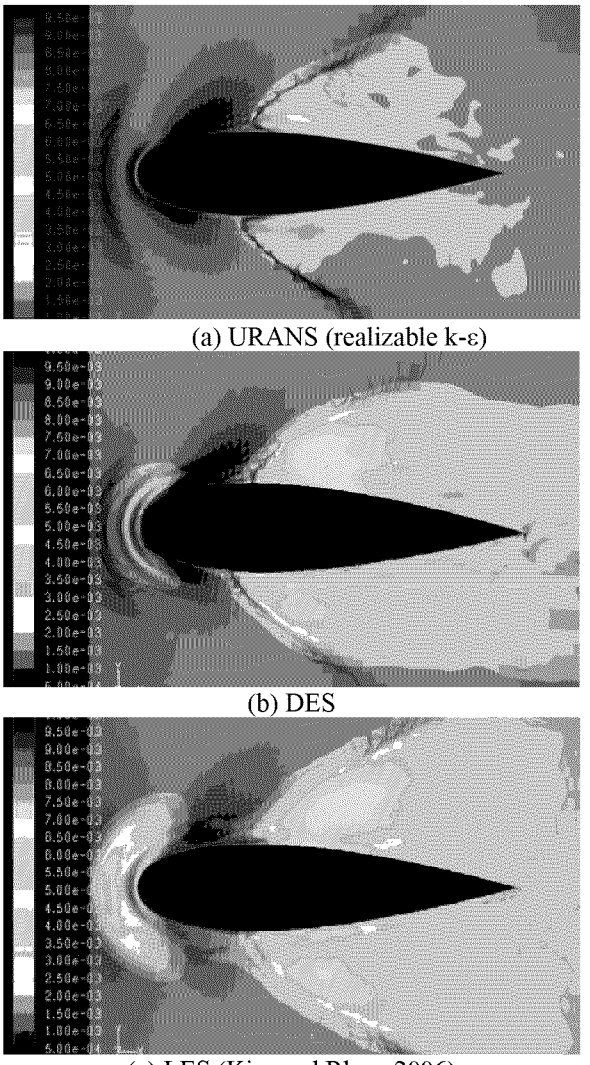

(a) URANS (realizable k-ε)

(b) DES

(c) LES (Kim and Rhee, 2006)

Figure 14. The r.m.s. wave height fluctuation predicted by the present URANS, DES, and LES at Fr = 0.37 with the coarse mesh

The capabilities of URANS, DES, and LES to reproduce transient aspects of the free-surface flows seem to widely vary. Figure 14 shows the contours of the r.m.s. free-surface elevation fluctuation predicted by the three different approaches. In lieu of being directly computed, the r.m.s. wave height fluctuation was estimated using:

$$\zeta' \equiv \frac{w'^2}{2g} \tag{13}$$

where ζ' is the r.m.s. wave height fluctuation and w' the r.m.s. vertical (z-) velocity fluctuation. In the earlier study (Kim and Rhee, 2006), the r.m.s. wave height fluctuation estimation using the LES had been found to be quite close to the measured r.m.s. data. Both the DES and the LES predictions are shown to yield largely the same degree of fluctuation. One notable difference between the DES and the LES results is that the LES gives a significantly large r.m.s. value in a larger portion of the free-surface. Furthermore, the LES prediction seems to pick the fluctuation in the bow region due to the spilling breakers and the capillary waves. The DES result is also indicative of the fluctuation at the bow, yet to a less degree. The URANS gives an insignificant fluctuation of the free-surface elevation.

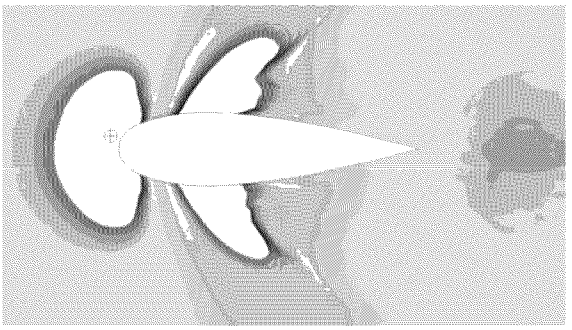

Figure 15. Locations of the three pressure probes in bow, separation, and flapping regions marked by circles

Figures 15 and 16 show the time histories of local static pressure signals and their spectra at three selected locations predicted by the DES and the LES on the fine mesh. The location of the pressure probes are marked with a circled "+" symbol in Figure 15: (i) bow-wave region; (ii) separated region; (iii) shoulder wave region outside the separated region. The spectra shown in Figure 16 for both the DES and the LES indicate that the pressure signals predicted are all largely broad-banded, yet showing distinct frequencies around which the power is concentrated.

The spectrum of the pressure signal at the bow predicted by the LES has a significant portion of power concentrated in high-frequency centered around 5 ~ 6 *Hz* most likely due to the weak spilling-breaker in the bow waves. The frequency range is quite close to the measured values of 7 *Hz* quoted by Metcalf *et al.*(2001) and 8.5 *Hz* reported by Metcalf *et al.*(2006) more recently. The spectra of the pressure signal at the separated shows pronounced peaks in the neighborhood of 2.0 *Hz*, which closely match the dominant frequency found in the experiment, f = 1.98 *Hz* (Metcalf *et al.*, 2006). The flapping region seems to be dominated by a low-frequency mode near f = 0.3 *Hz*, as clearly shown in both its spectrum. This frequency is also close to the measured one (f = 0.3 *Hz*). The DES predictions, overall, give a lower power density than the LES predictions over the entire frequency range for all three pressure signals.

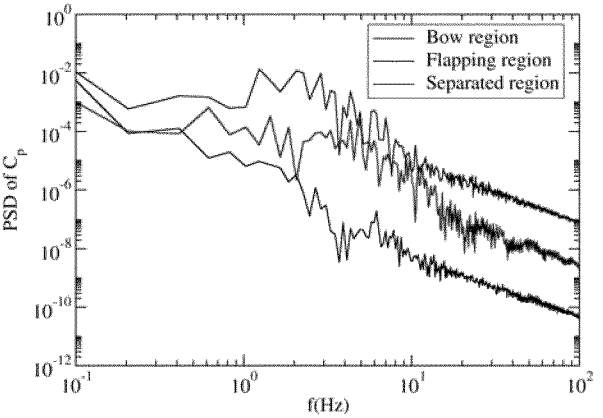

(a) DES

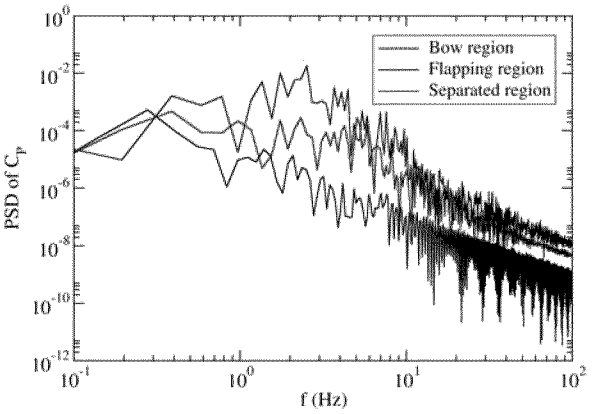

(b) LES (Kim and Rhee, 2006)

Figure 16. Power spectra of the local static pressure signals recorded at three different locations near the free-surface

Unsteady forces on the hydrofoil

The unsteadiness in the flow caused by the breaking waves and the large-scale turbulent structures in different regions of the flow leads to fluctuations in the resulting forces and moments on the hydrofoil surface. The oscillating forces and the moments can adversely affect the maneuvering

characteristics of surface vehicles such as directional stability, especially when the frequency of the oscillations in forces and moments falls in the neighborhood of the natural frequencies of the corresponding motions of vehicles.

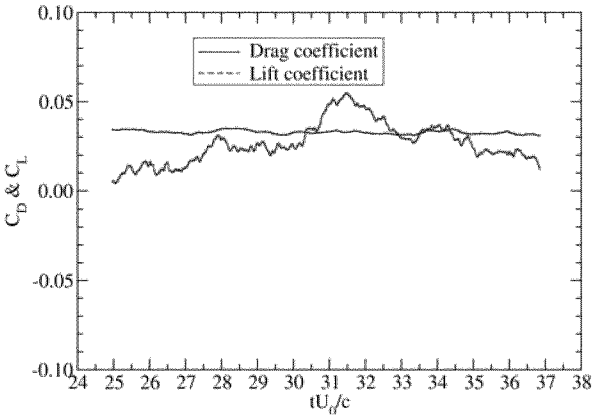

(a) DES

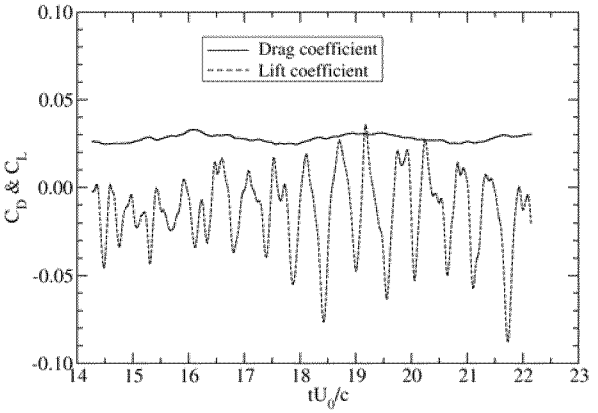

(b) LES (Kim and Rhee, 2006)

Figure 17. Time histories of the lift and drag coefficients: (a) DES prediction; (b) LES prediction

Figures 17(a) and 17(b) show the time histories of the drag and the lift coefficients predicted by the DES result along with the LES prediction. In the DES and the LES results alike, the drag coefficients oscillate with a fairly low frequency near $f = 0.3$ Hz, which is close to the dominant frequency of the pressure signal from the wave crest away from the hydrofoil (the region of flapping instability) discussed earlier. The most remarkable difference between the DES and the LES results lies with the lift coefficient. The lift coefficient predicted by the LES fluctuates with much larger amplitude than that from the DES. Also noteworthy in the history of the lift coefficients, for both the DES and the LES alike, is that, for the duration of time as shown in the plot, the time-averaged lift coefficients predicted by the DES and the LES appreciably deviate from zero. This aspect of the lift coefficient was discussed by Xing *et al.* (2006) and Kim and Rhee (2006).

SUMMARY, DISCUSSION, AND FUTURE WORK

In this study, a hybrid URANS/LES (DES) approach was attempted for the turbulent free-surface flows past two surface-piercing bodies. Our main focus was to evaluate the DES approach for turbulent free-surface flows involving wave-breaking and separation, and to compare the results against LES and RANS modeling approaches.

- The salient features of complex turbulent free-surface flows such as spilling-breaker at the bow along with the capillary waves, breaking of the shoulder waves, flow separation, splashing, and bubble formation are largely reproduced by the DES
- In the near-field, the DES yields less detailed flow features and a lesser degree of unsteadiness compared to the LES results. This is primarily due to the RANS turbulence model that is activated in the region, and is partly due to different subgrid-scale modeling in the DES approach adopted in this study.
- The quality of LES was found to degrade as the mesh becomes too coarse to resolve energy containing eddies. For the case of the hydrofoil, under-resolved LES led to a failure to capture the Kelvin waves away from the body where the mesh stretches rapidly. The DES, however, performed commendably, reproducing the Kelvin wave system.

ACKNOWLEDGMENT

The authors acknowledge that FLUENT was used for all the computations presented here.

REFERNCES

Brocchini, M. and Peregrine, D. H., "The Dynamics of Strong Turbulence at Free Surfaces, Part II Free-Surface Boundary Conditions," *J. Fluid Mech.*, Vol. 449, pp. 255 – 290, 2001.

Cokljat, D. and Liu, F. DES of Turbulent Flow Over an Airfoil at High Incidence," In 40th Aerospace Sciences Meeting and Exhibit, Reno, Nevada, USA, 14-17 January 2002. AIAA. paper 2002-0590.

Dommermuth, D. G. and Novikov, E. A., 1993, "Direct Numerical and Large-Eddy Simulation of Turbulent Free-Surface Flows," *6th Int'l Conf. On Numerical Ship Hydrodynamics, Iowa City*, 1993.

Drew, D. A.,"Mathematical Modeling of Two-Phase Flow," *Ann. Rev. Fluid Mech.*, ***15***, pp. 261 – 291, 1983.

Duncan, J. H. and Dimas, A. A., "Surface Ripples Due to Steady Breaking Waves," *J. Fluid Mech.*, Vol. 329, pp. 309 – 339, 1996.

Germano, M, Piomelli, U., Moin, P., and Cabot, W. H.,"Dynamic Subgrid Scale Eddy Viscosity Model," *Physics of Fluids* A, 3, **19**, pp. 1760 – 1765. 1991.

Harlow, E. H., and Welch, J. E., "Numerical Calculation of Time Dependent Viscous Incompressible Flow with Free Surface," *Physics of Fluids* **8**, pp. 2182-2189, 1965

Inoue, M., Baba, N., and Himeno, Y., J., 1993, "Experimental and Numerical Study of Viscous Flow Field around an Advancing Vertical Circular Cylinder Piercing a Free Surface,", *Kansai Soc. of Naval Architects of Japan*, Vol. 220, pp. 57 – 64.

Kandasamy, M., Wilson, R., and Stern, F., "RANS Simulation of Free-Surface Wave-Induced Separation Around a Surface-Piercing NACA0024 Hydrofoil," Presented at the 26th American Towing Tank Conference, Webb Institute, Glen Cove, New York, July 23 – 24, 2001.

Kandasamy, M., Xing, T., Wilson, R., and Stern, F., "Vortical and Turbulent Structures and Instabilities in Unsteady Free-Surface Wave-Induced Separation," *5th Osaka Colloquium on Ship Hydrodynamics*, Osaka, Japan, March 14 – 15, 2005,

Kawamura, T., Mayer, S., Garapon, A., and Sorensen, L., "Large Eddy Simulation of a Flow Past a Free Surface Piercing Circular Cylinder," *J. Fluids Eng.*, Vol. 124, pp. 91 – 101, 2002

Kim, S.-E., Makarov, B., and Caraeni, D., "Multi-Dimensional Reconstruction Scheme for Unstructured Meshes," AIAA Paper 2003-3990, 2003.

Kim, S.-E., "Large Eddy Simulation Using Unstructured Mesh and Dynamic Subgrid-Scale Turbulence Models," AIAA Paper 2004-2548, 2004.

Kim, S. E. and Makarov, B., "An Implicit Fractional-Step Method for Efficient Transient Simulation of Incompressible Flows," AIAA Paper 2005-5253, Presented at 17th AIAA Computational Fluid Dynamics Conference, June 6 – 9, Toronto, Ontario, 2005.

Kim, S. E. and Rhee, S. H., 2006, "Large Eddy Simulation of Turbulent Free Surface Flow Around Surface-Piercing Bodies the 26th Symposium on Naval Hydrodynamics, September 17 – 22, Rome, Italy.

Mary, I. and Sagaut, P., "Large eddy simulation of flow around an airfoil near stall," AIAA J. VOl. 40, No. 6, pp.113 - 1145, 2002.

Menter, F.R., Kuntz, M., and Langtry, R., "Ten years of industrial experience with the SST turbulence model," In K Hanjalic, Y Nagano, and M Timmers, editors, Turbulence, Heat and Mass Transfer, 4, pp. 625 – 632, Begell House, Inc., Begell House, Inc., 2003.

Metcalf, B., Longo, J, and Stern, F., "Experimental Investigation of Wave-Induced Boundary Layer Separation Around a Surface-Piercing NACA 0024 foil: Towing Tank Experiment," Presented at the 26th American Towing Tank Conference, Webb Institute, Glen Cove, New York, July 23 – 24, 2001.

Metcalf, B., Longo, J, Ghosh, S., and Stern, F., "Unsteady Free Surface Wave Induced Boundary Layer Separation for a Surface-Piercing NACA 0024 foil: Towing Tank Experiment," *J. Fluids and Structures*, **22**, pp. 77 – 98, 2006.

Nikitin, N.V, Nicoud, F., Wasistho, B. Squires, K.D. and Spalart, P.R., "An approach to wall modeling in large-eddy simulations," *Phys. Fluids*, 12(7):1629.1632, 2000.

Pogozelski, E. M. and Katz, J., "The Flow Structure Around a Surface Piercing Strut," *Physics of Fluids*, **9(5)**, pp. 1387 – 1399, 1997.

Rhee, S. H. and Makarov, B., "Validation Study for Free-Surface Wave Flows Around Surface-Piercing Cylindrical Structures," Proceedings of OMAE2005, 24th International Conference on Offshore Mechanics and Arctic Engin., Halkidiki, Greece, June 12 – 17, 2005,

Shen, L. and Yue, D. K. P., "A Large Eddy Simulation of Free-Surface Turbulence," *J. Fluid Mech.*, Vol. 440, pp. 75 – 116, 2001.

Shen, L., Zhang, C. and Yue, D. K. P., "Free-Surface Turbulent Wake Behind Towed Ship Models: Experimental Measures, Stability Analysis and Direct Numerical Simulations," *J. Fluid Mech.*, Vol. 469, pp. 89 – 120, 2002.

Shih, T.H., Liou, W.W., Shabbir, A., Yang, Z., and Zhu, J., "A New Eddy-Viscosity Model for High Reynolds Number Turbulent Flows - Model Development and Validation," *Computers & Fluids*, 24(3):227-238, 1995.

Spalart, P.R., Jou, W.H., Strelets, M., and Allmaras. S.R., "Comments on the Feasibility of LES for

Wings, and on a Hybrid RANS/LES Approach," In C Liu and Z Liu, editors, First AFOSR International Conference on DNS & LES,. Greyden Press, August 1997.

Spalart, P.R., Hedges, L. and Shur, M., "Simulation of Active Flow Control on a Stalled Airfoil," *Flow Turb. Comb*., 71:361.373, 2003.

Strelets, M., "Detached-Eddy Simulation of Massively Separated Flows," AIAA, 2000. Paper 2001-0879.

Sussman, M., Smereka, P., and Osher, S, "A Level Set Approach for Computing Solutions to Incompressible Two-Phase Flow," *J Comp Physics* **114**, pp. 146-159, 1994.

Travin, A., Shur, M., Strelets, M., and Spalart, P., "Detached-eddy Simulations Past a Circular Cylinder," *Flow Turb. Comb*., 63:293.313, 2000.

Xing, T., Kandasamy, M., and Stern, F., "Unsteady Free-Surface Wave Induced Separation,: Analysis of Turbulent Structures Using Detached Eddy Simulation and Single-Phase Level-Set," *In Preparation for a Journal Publication*, 2006.

Xing, T., Kandasamy, M., Wilson, R., and Stern, F., "DES and RANS of Unsteady Free-Surface Wave Induced Separation," AIAA Paper 2004-0065, Presented at the 42nd Aerospace Sciences Meeting & Exhibit, Reno, NV, Jan. 5 – 8, 2004.

Yue, W., Lin, C.-L., and Patel, V.C., "Large Eddy Simulation of Turbulent Open-Channel Flow with Free-Surface Simulated by Level-Set Method," *Physics of Fluids*, **17**, 2005.

Zhang, Z. L. and Stern, F., "Free-Surface Wave-Induced Separation,"*ASME J. Fluids Eng.*, Vol. 118, pp. 546 – 554, 1996.